Series of alternating states with unpolarized and spin-polarized bands in dimerized IrTe$_2$

G. L. Pascut,[1] T. Birol,[1] M. J. Gutmann,[2] J. J. Yang,[3] S.-W. Cheong,[1,3,4] K. Haule,[1] and V. Kiryukhin[1,4]

[1]*Department of Physics and Astronomy, Rutgers University, Piscataway, New Jersey 08854, USA*
[2]*ISIS Facility, STFC-Rutherford Appleton Laboratory, Didcot OX11 OQX, United Kingdom*
[3]*Laboratory of Pohang Emergent Materials and Department of Physics,*
Pohang University of Science and Technology, Pohang 790-784, Korea
[4]*Rutgers Center for Emergent Materials, Rutgers University, Piscataway, New Jersey 08854, USA*

A series of states with different densities of stripes of Ir dimers is investigated using x-ray diffraction and density functional theory in layered nonmagnetic metal IrTe$_2$. With decreasing temperature, structures with and without inversion symmetry alternate. In noncentrosymmetric states, spin-orbit coupling splits the electronic energy bands into spin-polarized pairs. Factors affecting the stability of the observed dimerized states are established, and it is conjectured that an infinite series of alternating states with and without polarized bands is realized in IrTe$_2$. Switching dimerized states with different symmetries by changing temperature or strain enables control of band polarization, adding a new tool for spintronics and valleytronics research.

I. INTRODUCTION

Compounds with large spin-orbit coupling (SOC) have recently attracted significant attention because of numerous exotic phenomena, such as $J_{\text{eff}} = 1/2$ Mott state [1], and topological insulators [2]. In nonmagnetic compounds, a combination of time reversal and inversion symmetries makes spin-up and spin-down states in electronic energy bands degenerate, leading to zero band polarization. One of the remarkable consequences of SOC is the splitting of electronic energy bands into spin-polarized pairs in compounds that lack inversion symmetry [3] [polarization direction varies over the Brillouin zone (BZ), generally]. This mechanism does not rely on any conventional magnetic interactions, and therefore works in both magnetic and nonmagnetic compounds. Polarized electronic bands are recognized for their importance for spintronic applications [4], as well as for other exotic phenomena, such as mixed singlet/triplet superconductivity [5], and intrinsic spin-Hall effect [6]. They may also be relevant for valleytronics research [7,8] (through affecting polarization of valley pseudospins). Controlling the polarized bands using nonmagnetic mechanisms is of clear importance for these applications.

Spin-orbit coupling is largest in heavy elements. Among heavy-metal compounds, hexagonal layered materials attracted increasing interest as systems with potentially applicable large polarized band splitting (e.g., BiTeI) [9], and as model valleytronics compounds [7]. IrTe$_2$ is a hexagonal layered metal composed of stacked layers of IrTe$_6$ octahedra forming a CdI$_2$-type structure at $T = 300$ K [10]. Triangular Ir and Te layers are stacked along the c_0 hexagonal axis. For $T < T_S = 280$ K, a modulated structure characterized by the wave vector $q_1 = (1/5, 0, 1/5)$ has been found in transmission electron microscopy [11] and x-ray studies [12] (q_n is quoted with respect to the $T = 300$ K unit cell). Scanning tunneling microscopy (STM) measurements [13] suggest that a series of coexisting structures with wave vectors $q_n = [1/(3n + 2), 0, 1/(3n + 2)]$, $n = 1, 2, 3 \ldots$ occurs, with n increasing as temperature decreases. The $n = 1$ structure has

been determined using x-ray diffraction [12]. It consists of stripes of Ir dimers (20% Ir-Ir bond length contraction) in the Ir planes, see Fig. 1(d). The stripes are stacked in a staircase-type pattern along the c_0 axis, generating the triclinic unit cell shown in Fig. 1(g). A complex pattern of Te displacements is realized in the Te layers, with dimerlike structures located near the Ir dimers. The Ir dimers form "walls" cutting through the structural Ir and Te layers, see Fig. 1(g). These walls exhibit reduced density of states (DOS) at the Fermi level E_F, giving rise to a quasi-two-dimensional (2D) electronic state "tilted" with respect to the hexagonal c_0 axis [12]. The corresponding Fermi surface (FS) is shown in Fig. 1(j). Density functional theory (DFT) calculations show that the Ir-Ir bonds in the dimers possess a covalent character, indicating that the Ir dimerization is the driving force of the structural transition [12]. Alternative mechanisms emphasizing the role of the Te orbitals [14–16], as well as a charge density wave scenario [17] have also been proposed. Spin-orbit coupling was found to disfavor the dimerized state, and the only effect of SOC discussed so far is a possible reduction of the T_S [12].

Probable schematic patterns of the Ir dimerization for $n > 1$ were proposed in STM studies [13]. These patterns are conjectured from the shifts of the Te atoms on the surface of the cleaved sample, which exposes the Te layer. However, the actual crystallographic structures, and even the values of q_n in the c_0 direction remained unknown. Herein, we report x-ray diffraction studies of the $n = 2,3,4$ and $n = \infty$ states in single crystals of pure and Se-doped IrTe$_2$. The atomic positions are determined for two structures: $n = 2$ with $q_2 = (1/8, 0, 1/8)$, and $n = \infty$. As explained later, $q_\infty = (1/6, 0, 1/6)$. Using the experimentally observed structures and DFT, we propose the dimerization patterns for the entire series and find that inversion symmetry is absent for even n. We show that significant SOC-induced splitting of polarized electronic bands occurs in the latter states and propose a tentative temperature-strain phase diagram containing alternating states with polarized and unpolarized bands.
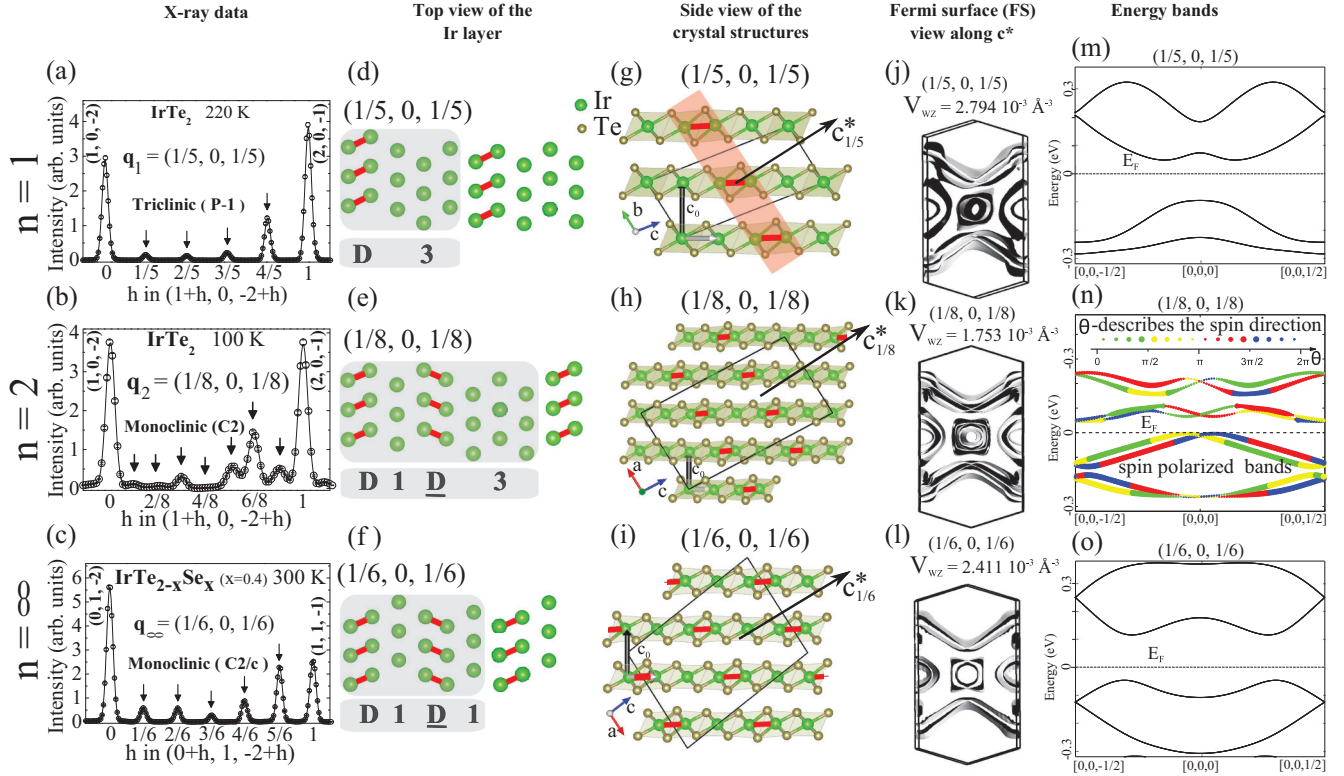
FIG. 1. (Color online) Three horizontal rows refer to the $n = 1, 2$, and ∞ states, respectively. (a)–(c) X-ray diffraction scans showing the q_n Bragg peaks. Experimental temperatures, sample compositions, and the symmetry of the crystal structures are indicated. (d)–(f) Dimerization patterns in the Ir planes. (g)–(i) Side views of the crystal structures. Solid lines show the unit cells. Crystallographic axes a, b, c, the reciprocal axes c^*, and the high-T hexagonal axes c_0 are shown with arrows. Thick lines mark the Ir dimers. Ir dimer "wall" is shown with tilted shaded rectangle in (g). (j)–(l) Calculated Fermi surfaces, as viewed along the c^* direction. V_{WZ} give the volume of the Wigner-Seitz cells. (m)–(o) Calculated energy bands in the $[0, 0, l]$ direction (along the c^*). The shown $\pm[0, 0, 0.5]$ wave vector range becomes $\pm(1/2p, 0, 1/2p)$, $p = 3n + 2$, in the high-temperature notation. In panel (n), the spin directions in the polarized bands are color-coded using the angle θ with respect to the c axis. The spins are confined in the ac plane for the bands shown.

II. EXPERIMENTS

Single crystals of IrTe$_{2-x}$Se$_x$ ($x = 0, 0.4$) were grown using Te flux, as described in Ref. [18]. Samples from the same batches as those described in Refs. [13,18] were used, and their bulk properties can be found there. X-ray diffraction measurements were done at different temperatures (300, 220, 100 K) using an Oxford Diffraction SuperNova Diffractometer equipped with a charge-coupled device (CCD) detector, a nitrogen gas cooler, and Mo K_α radiation. Data collection, cell refinement, and data reduction were carried out using CrysAlisPro [19]. Superflip software [20] was used for structure solution and space group assignment, and Jana2006 [21] for structure refinement. Crystal structure figures were generated using VESTA [22]. The absorption correction was done analytically using a multifaceted crystal model [23]. No extinction corrections were necessary.

The IrTe$_2$ samples used in this paper exhibit two visible first-order transitions in electrical resistivity measurements on cooling, the first one around $T_S = 280$ K, and the second one at $T_{S1} = 180$ K, see Ref. [13]. In our x-ray measurements, appearance of the $n = 1, 2$, etc. states is indicated by emergence of the q_n Bragg peaks. We find that in a single cooling run

(no thermal cycling), the pure $n = 1$ phase is present for $T_{S1} < T < T_S$, see Fig. 1(a), while this phase coexists with the $n = 2$ phase for $T < T_{S1}$. The STM measurements of Ref. [13] indicate that, on warming from temperatures below T_{S1}, the samples remain in such a coexisting state all the way up to T_S. However, we were able to obtain the pure $n = 2$ state in IrTe$_2$ samples at $T = 100$ K using thermal cycling. The sample was first cooled from $T \sim 400$ K down to $T = 100$ K and kept at this temperature for about an hour. It was then warmed above T_{S1} up to $T = 200$ K and kept there for another hour. Finally, the sample was cooled down to $T = 100$ K, and the pure $n = 2$ phase was observed, see Fig. 1(b).

Different thermal cycling protocols lead to the appearance of larger n states, with volume fractions depending strongly on the thermal history. The $n = 4$ and ∞ phases (see Fig. 2), as well as evidence for the $n = 3$ state, were found in the x-ray diffraction data. No states violating the $1/(3n + 2)$ rule were observed. The system is strongly hysteretic, consistent with the reported first-order transition type [10,11,13], and the large n states survive at elevated temperatures. Traces of the $n = 4$ state, for example, were detected at $T = 220$ K. The equilibrium transition temperatures are, therefore, impossible to determine from our data. As described above, we were
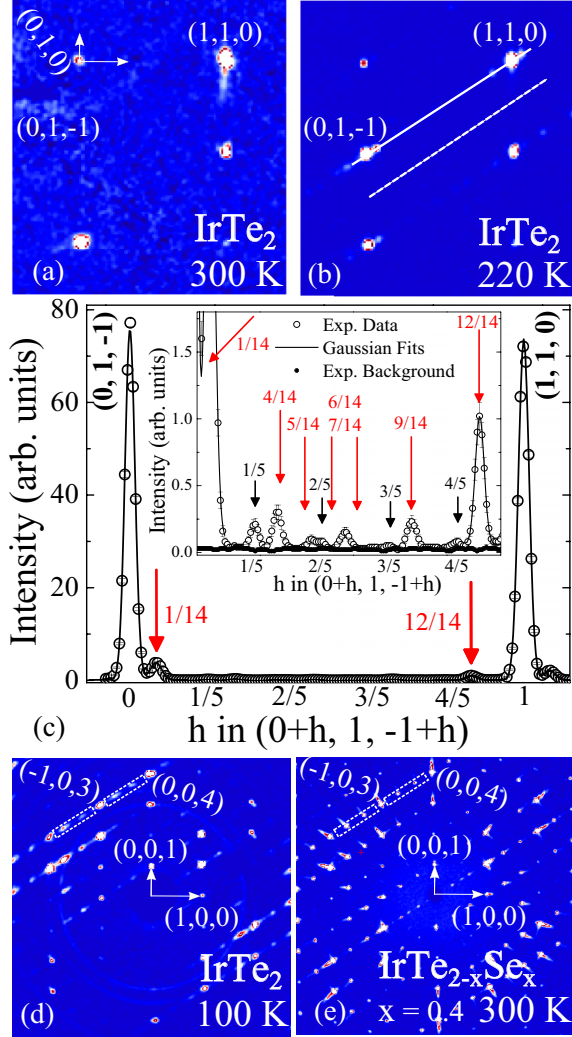
FIG. 2. (Color online) X-ray diffraction patterns in the $(H, 1, L)$ reciprocal plane of $IrTe_2$ at (a) $T = 300\,K$ and (b) $T = 220\,K$ after thermal cycling. (c) One-dimensional cut (open circles) in this plane for $T = 220\,K$ taken along the white solid line in panel (b). Experimental background taken along the dashed line in (b) is shown with filled circles. Black solid line is a guide for the eye. The superlattice peaks due to the $n = 1$ and $n = 4$ phases are shown with short and long arrows, respectively. The diffraction patterns in the $(H, 0, L)$ planes for (d) $IrTe_2$ at $T = 100\,K$ and (e) $IrTe_{1.6}Se_{0.4}$ at $T = 300\,K$. The superlattice peaks due to the $n = \infty$ phase with $q_\infty = (1/6, 0, 1/6)$ are present in both (d) and (e), as can be seen, for example, in the boxed areas. In all panels, reciprocal space positions are given in the high-temperature notation.

TABLE I. Experimental atomic parameters for the $n = 2$ phase in $IrTe_2$ at 100 K obtained from single crystal x-ray diffraction. The structural model was fitted against 1924 unique reflections satisfying $|F| > 3\sigma(|F|)$ with the full-matrix least-squares on $|F|$ refinement method ($R_1 = 0.133$). The atomic positions are given in the lattice parameter units. The space group is $C2$ (No. 5); the unit cell parameters are $a = 12.7036(13)\,\text{Å}$, $b = 3.9646(3)\,\text{Å}$, $c = 22.6796(18)\,\text{Å}$, $\alpha = 90°$, $\beta = 92.642(7)°$, $\gamma = 90°$.

Atom	Site	x	y	z	$U_{iso}\,(\text{Å}^2)$
Ir1	2a	0	0.0000(11)	0	0.00143(20)
Ir2	4c	0.23031(16)	0.4979(7)	0.25834(9)	0.00143(20)
Ir3	2b	0	0.6623(10)	0.5	0.00143(20)
Ir4	4c	0.36641(16)	0.0003(8)	0.12729(8)	0.00143(20)
Ir5	4c	0.13627(16)	0.1774(7)	0.36890(9)	0.00143(20)
Te1	4c	0.0952(4)	0.0033(14)	0.25731(16)	0.0017(2)
Te2	4c	0.8633(4)	0.4991(14)	0.00985(16)	0.0017(2)
Te3	4c	0.3682(4)	0.0029(13)	0.24325(14)	0.0017(2)
Te4	4c	0.0019(4)	0.0037(13)	0.11554(14)	0.0017(2)
Te5	4c	0.2308(4)	0.5016(14)	0.13963(16)	0.0017(2)
Te6	4c	0.4971(4)	0.1697(13)	0.38329(16)	0.0017(2)
Te7	4c	0.1346(4)	0.1647(13)	0.48668(16)	0.0017(2)
Te8	4c	0.2296(4)	0.1665(13)	0.63132(16)	0.0017(2)

III. FIRST-PRINCIPLES CALCULATIONS

Density functional theory calculations were carried out to (i) analyze the origin of the observed sequence of states by performing relaxation of the structures and testing their stability, and (ii) calculate the band structure and FS. Two different calculation schemes were employed. For the band structure and FS, SOC is of key importance, especially for the electronic band polarization effects. Thus, the WIEN2k package [24] [generalized gradient approximation Perdew-Burke-Ernzerhof (GGA-PBE) functional [25]] with SOC included was used for these calculations. In contrast, SOC and strain effects were shown to play a secondary role when it comes to the stability of the dimerized $n = 1$ structure [12]. To test different DFT methods with respect to the stability of the experimentally seen dimerization patterns, we have performed atomic relaxations using the following combinations: (i) GGA-PBE [25] or local density approximation (LDA) [26] for the exchange-correlation functional; (ii) with or without SOC; (iii) using the experimental or unstrained unit cells (unit cell construction is discussed in detail in the Appendix). The obtained atomic positions in the relaxed structures were found to be practically independent on the specific combination of (i), (ii), and (iii) used. We have also carried out these calculations for the artificially created dimerization patterns described below, and the obtained results were independent on the DFT method used, too. Therefore, the economical scheme utilizing the fast Vienna *Ab initio* Simulation Package (VASP) code [27] with GGA-PBE exchange-correlation functional was chosen, SOC was not included, and unstrained unit cells were used. The starting dimerized patterns of the artificial structures described below were created manually with the dimer distances similar to those obtained from experiment. During the relaxations of atomic positions for the artificially created dimerized patterns, many of the structures were unstable, i.e., converged to the

able to obtain the pure $n = 1$ and $n = 2$ states in $IrTe_2$. After numerous attempts, we were unable to identify the thermal protocol leading to the pure $n = \infty$ phase in the whole volume of the undoped $IrTe_2$. Therefore, we studied this state in the $x = 0.4$ Se-doped sample, in which the q_∞ wave vector was observed at $T = 300\,K$, see Fig. 1(c). The $n = 2$ ($x = 0$) and $n = \infty$ ($x = 0.4$) structures were determined from the diffraction data. The obtained atomic coordinates and isotropic thermal parameters are given in Tables I and II. The $n = 1$ structure is described in Ref. [12].

TABLE II. Experimental atomic parameters for the $n = \infty$ phase in $IrTe_{2-x}Se_x$ ($x = 0.4$) at 300 K obtained from single crystal x-ray diffraction. The structural model was fitted against 1954 unique reflections satisfying $|F| > 3\sigma (|F|)$ with the full-matrix least-squares on $|F|$ refinement method ($R_1 = 0.055$). The atomic positions are given in the lattice parameter units. *Occ* stands for site occupancy. The space group is $C2/c$ (No. 15); the unit cell parameters are $a = 12.6659(6)$ Å, $b = 3.92240(10)$ Å, $c = 16.9186(7)$ Å, $\alpha = 90°$, $\beta = 99.283 (4)°$, $\gamma = 90°$.

Atom	Site	x	y	z	U_{iso} (Å^2)	*Occ*
Ir1	$4e$	0	0.08032(15)	0.25	0.00884(10)	1
Ir2	$8f$	0.31705(3)	0.09017(11)	0.07356(2)	0.00917(8)	1
Te1	$8f$	0.36061(6)	0.0795(2)	0.23225(4)	0.00978(16)	0.793(9)
Te2	$8f$	0.31710(6)	0.0823(2)	0.42469(4)	0.01082(17)	0.812(9)
Te3	$8f$	0.03864(6)	0.0832(2)	0.40262(4)	0.00976(16)	0.793(9)
Se1	$8f$	0.36061(6)	0.0795(2)	0.23225(4)	0.00978(16)	0.207(9)
Se2	$8f$	0.31710(6)	0.0823(2)	0.42469(4)	0.01082(17)	0.188(9)
Se3	$8f$	0.03864(6)	0.0832(2)	0.40262(4)	0.00976(16)	0.207(9)

undimerized high-temperature structure. In these cases, the Ir pattern was fixed and the Te positions relaxed to obtain the "best" Te positions for this pattern. The Ir and Te positions were then relaxed separately, one after another, until the procedure converged, in a search for a possibly missed local energy minimum.

IV. DISCUSSION

The experimentally obtained Ir dimerization patterns for the $n = 1, 2$ and ∞ states are shown in Figs. 1(d)–1(f). They consist of stripes of dimers, designated D or $\underline{D}$ in the figures, depending on which of the two possible dimerization types (dimer tilts) within the stripe is chosen. The stripes are separated by either one or three columns of undimerized Ir atoms, designated 1 and 3, respectively. Inspection of these patterns reveals that the in-plane q_n periodicities can be naturally generated by repeating n dimerized stripes separated by 1, and ending the unit cell sequence with 3. The dimer stripe type (D or $\underline{D}$) changes across 1. Thus, using these empirical rules, one gets D3 [Fig. 1(d)], D1$\underline{D}$3 [Fig. 1(e)], D1$\underline{D}$1D3, etc. for the $n = 1, 2, 3, \ldots$ states, obtaining the correct in-plane periodicity of $3n + 2$ Ir columns. In other words, the pattern consists of n alternating D1 and $\underline{D}$1 blocks, capped by the 2 block, see Fig. 4(a). The fraction of dimerized Ir increases with n until the maximum dimer density consistent with the above rules is reached in the $n = \infty$ state, D1$\underline{D}$1 [Fig. 1(f)] with 6 Ir columns in the repeating unit. The dimerized IrTe$_2$ layers are stacked in the staircaselike pattern, giving rise to the unit cells shown in Figs. 1(g)–1(i) and explaining the observed three-dimensional $q_n = [1/(3n + 2), 0, 1/(3n + 2)]$, with $q_\infty = (1/6, 0, 1/6)$.

To analyze the origin of the observed sequence of states, DFT calculations (relaxation of the structures) were carried out using the VASP code as described above. All the experimental structures are well reproduced by DFT, with atomic positions deviating by less than 1% from their measured positions (in the lattice parameter units). In addition to the experimental structures, other possible in-plane patterns containing dimerized stripes were constructed to test their stability as follows. A given in-plane $3n + 2$ periodicity can hold N stripes, $1 < N < N_{max}$, $N_{max} = (3n + 2)/2$ for even n, and

$(3n + 1)/2$ for odd n. By considering all the arrangements of the stripes giving the $3n + 2$ periodicity for the allowed N, all the possible in-plane combinations were obtained. Stacking the Ir planes in a staircaselike pattern, the unit cells similar to those of Figs. 1(g)–1(i) were produced. Within these fixed unit cells, the initial high-temperature structure with imposed Ir dimerization pattern was relaxed fully. The details of unit cell construction can be found in the Appendix. The full set of the in-plane dimerized patterns for the experimentally relevant periodicities is shown schematically in the legend to Fig. 3. The obtained results can be summarized as follows: (i) Fully dimerized structures (DD, D$\underline{D}$, etc.), as well as states containing D1D and D2D blocks, are unstable. They are prohibited by high elastic energy cost, as explained later. (ii) Dimers of the opposite type separated by 1 or 2 undimerized Ir columns (D1$\underline{D}$1, D2$\underline{D}$1, etc.), and the states in which the dimers of any type are separated by more than two columns are stable. All the experimental structures known so far from x-ray (Fig. 1) and STM [13] measurements exhibit the maximum dimerized stripe densities allowed by these rules for a given unit cell size, probably due to the energy gain from the formation of Ir-Ir covalent bonds in the dimers [12]. Rules (i) and (ii), combined with the maximum allowed dimer density requirement produce the $3n + 2$ periodicity observed in experiments. For odd n, only the pattern shown in Fig. 4(a) is possible. For even n, two end patterns, . . . D1$\underline{D}$3 and . . . D2$\underline{D}$2, are allowed by these rules. Experimentally, the D1$\underline{D}$3 pattern is realized for the $n = 2$ case. It also has the lower energy (by 5–10 meV/f.u.) in the DFT calculations for the $n = 2$ and 4 states. Thus, although DFT calculations are designed for zero temperature, they successfully reproduce the experimentally observed structures ($n = 1, 2, \infty$), provided that the index n (unit cell size) is given. They also predict that the pattern of Fig. 4(a) holds for at least $n = 3$ and 4, suggesting that it might continue for larger n. To strengthen the DFT predictions, especially for even n, temperature effects should be taken into account, and more realistic models including entropy and, possibly, kinetics should be used. The total energies for the experimental structures for various DFT methods are given in the Appendix. In agreement with the previous report [12] for $n = 1$, DFT favors the undistorted state
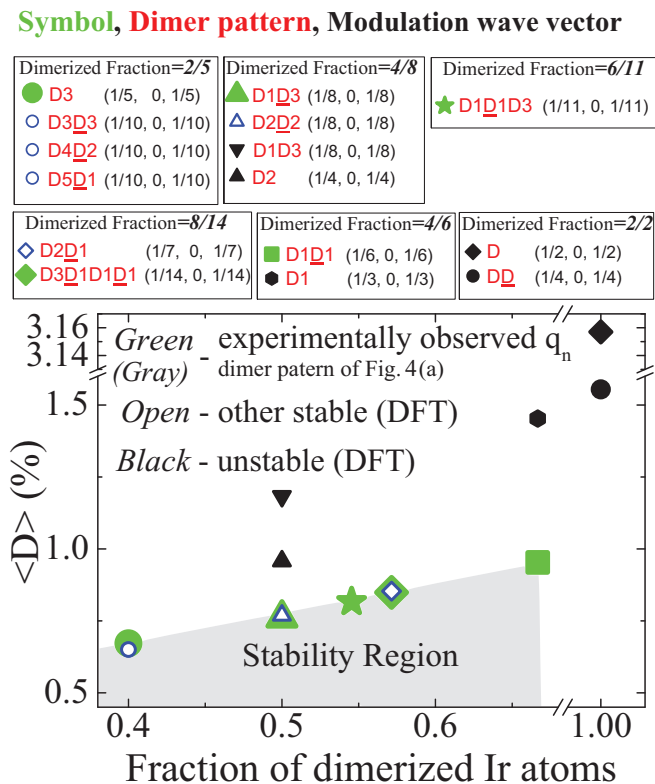
FIG. 3. (Color online) Baur distortion index $\langle D \rangle$ of the $IrTe_6$ octahedra for the experimental and theoretical dimer patterns with various fractions of dimerized Ir atoms. Large green (gray) symbols designate the patterns proposed in Fig. 4(a), shown for all the observed wave vectors q_n. These patterns are experimentally confirmed for $n = 1, 2, \infty$. The other patterns are designated by the open symbols for the states stable within DFT, and by the filled black symbols for the unstable states. The in-plane dimerization patterns and the corresponding q_n are given in the legend on top of the figure. The dimerization pattern notation is described in the text.

FIG. 4. (Color online) (a) The proposed dimerization pattern for a state with modulation wave vector q_n (confirmed experimentally for $n = 1, 2$, and ∞). (b) Tentative schematic equilibrium phase diagram of $IrTe_{2-x}Se_x$. The horizontal axis can be understood as generalized compressive strain. Large dots indicate experimentally determined structures. Structures up to $n = 4$ were observed. The phases are identified using the in-plane modulation vector $1/(3n + 2)$. The noncentrosymmetric $1/8$ phase ($n = 2$) is marked with NCS.

over the dimerized structures. Thus, as pointed out previously [12], determination of the true ground state among all the q_n structures appears to be beyond the reach of DFT, probably because DFT underestimates the nonlocal energy gain due to the Ir dimerization. This suggestion is consistent with the maximum dimer density requirement discussed above. Application of nonlocal methods, such as cluster dynamical mean field theory, could resolve this issue. Thus, state-of-the-art calculational methods are required to better understand the competition between the dimerized phases. Such calculations are highly desirable, in our opinion.

To gain insight into the DFT results and answer questions such as why the complete Ir dimerization is impossible, we note that the energy gain due to the Ir dimerization competes with the elastic energy loss. To characterize this loss roughly, it is sufficient to consider deformation of the strongest bonds in the system: the Ir-Te bonds. These bonds are the shortest (~ 1.65 Å) and exhibit both the ionic and covalent character. The Ir-Ir and Te-Te in-plane bonds are much longer (~ 3.9 Å), virtually approaching the sum of the atomic van der Waals radii (~ 4.1 Å). The interplane Te-Te bonds are also weak (this is the cleavage plane [13]). The quantitative measure of the
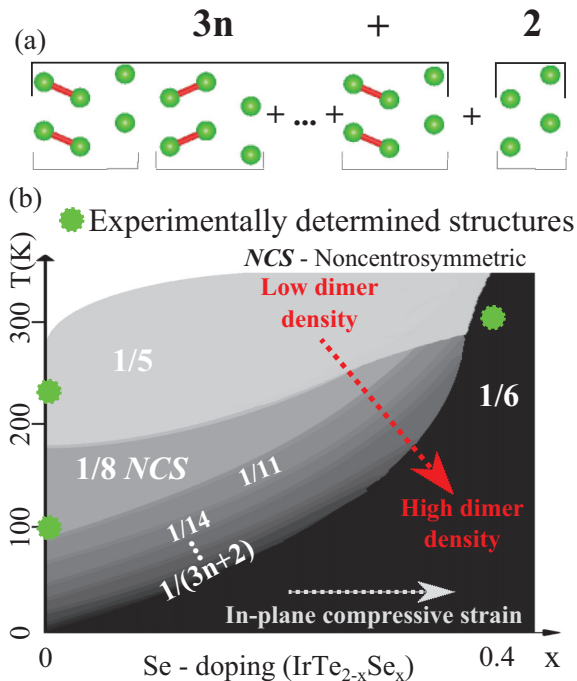
Ir-Te bond distortion is the Baur index [28] $\langle D \rangle$, defined as $\sum_{i=1}^{6} |l_i - l_{av}|/6l_{av}$ calculated for each $IrTe_6$ octahedron (l_i and l_{av} are the individual and the average Ir-Te bond lengths, respectively), and then averaged over all the octahedra in the unit cell. Figure 3 shows $\langle D \rangle$ for all the experimental and artificial dimer patterns considered in our study. For unstable states, $\langle D \rangle$ was calculated for the structures with imposed fixed Ir dimerization (~ 3.2 Å Ir-Ir dimer bond length), and DFT-relaxed Te positions. For a given dimer density (and the associated dimerization energy gain), the Baur index of the unstable structures is always significantly larger than that of the stable ones (Fig. 3). The nonexistent fully dimerized states exhibit very large $\langle D \rangle$. Thus, the elastic energy cost is prohibitively large for the states unstable within DFT, including the fully dimerized states.

For the band structure and FS calculations, SOC is of key importance, especially for the electronic band polarization effects. Thus, the WIEN2k package (GGA-PBE functional) with SOC included was used for these calculations. Band polarization was calculated for the noncentrosymmetric $n = 2$ structure. As was previously reported for the $n = 1$ case [12], the experimental $n = 2$ and ∞ states contain "walls" of Ir dimers cutting diagonally through the structural Ir and Te layers, see Figs. 1(g)–1(i). These walls exhibit reduced DOS at E_F, giving rise to a quasi-2D electronic state, with electronic planes normal to the reciprocal c^* axes. The corresponding calculated quasi-2D FS are shown in Figs. 1(j)–1(l).

TABLE III. Theoretical atomic positions for the $n = \infty$ phase in IrTe$_2$ obtained from first-principles calculations. These positions were obtained by assuming that IrTe$_2$ has the same lattice parameters as IrTe$_{2-x}$Se$_x$ ($x = 0.4$) given in Table II, and then fully relaxing the atomic positions of both Ir and Te ions. The atomic positions are given in the lattice parameter units.

Atom	Site	x	y	z
Ir1	$4e$	0	0.08350	0.25
Ir2	$8f$	0.31575	0.09467	0.07299
Te1	$8f$	0.35808	0.08289	0.23304
Te2	$8f$	0.32077	0.08786	0.42331
Te3	$8f$	0.03692	0.08762	0.40725

Experimental atomic coordinates were used for $n = 1,2$. To avoid difficulties due to fractional Se doping, the FS for the $n = \infty$ case was calculated using theoretical coordinates of the pure IrTe$_2$ structure relaxed under the experimentally determined symmetry and the unit cell; see Table III. The geometry of these FS (tilted with respect to the structural planes) is highly unusual. Direct confirmation of this geometry (e.g., in de Haas–van Alphen experiments) would be of significant interest.

An important result of our x-ray experiments is that the $n = 1$ and ∞ crystallographic structures exhibit inversion symmetry (space groups P-1 and $C2/c$, respectively), while the $n = 2$ state lacks it (space group $C2$). In noncentrosymmetric structures, SOC splits the electronic bands into spin-polarized pairs [5]. Figures 1(m)–1(o) show examples of the calculated band structures for the experimental $n = 1,2$ and ∞ states. The bands are split only for $n = 2$, with polarized band splittings as large as $\sim$100 meV observed throughout the BZ, consistent with the large SOC of Ir ($\sim$0.5 eV). The $n = 2$ bands are spin-polarized, with the polarization varying over the BZ, as shown in Fig. 1(n). The in-plane Ir dimerization patterns shown in Figs. 1(d)–1(f) clearly possess the inversion symmetry for the $n = 1,\infty$ cases, and lack it for the $n = 2$ case. It can be easily seen that the corresponding patterns for the $n > 2$ states constructed according to the D1$\underline{D}$1 . . 2 rule [Fig. 4(a)] proposed above have the inversion symmetry for odd n, and lack it for even n. Thus, it is natural to conjecture that the even n states possess split polarized bands, while the odd n states do not. Experimental testing of this proposal for $n > 2$ is the subject of future work.

Compressive in-plane strain should favor the dimerized state. Indeed, moderate Se doping is known to produce the maximally dimerized $n = \infty$ state for all temperatures below the structural transition [18]. Thus, the Ir dimerization patterns can be switched not only by temperature, but by strain. The published [18] phase diagram of IrTe$_{2-x}$Se$_x$ lacks the $n = 2,3$, etc. states and therefore is incomplete. Unfortunately, due to the first-order character of the structural transitions in IrTe$_2$, establishing the equilibrium phase diagram is very difficult. On cooling the pure IrTe$_2$, the $n = 1$ state appears first in our experiments, then the $n = 2$ state, and then the larger n states, generally in a phase mixture. It is reasonable to propose that these states appear consecutively in an equilibrium phase diagram. Based on this conjecture and on the phase diagram

of Ref. [18], we propose a tentative equilibrium temperature-strain phase diagram shown in Fig. 4(b). In this diagram, states with and without the inversion symmetry alternate if the pattern of Fig 4(a) holds, and the splitting of the polarized energy bands can be switched on and off by either temperature or strain. We believe that experimental determination of the actual phase diagram is highly desirable and might provide a rare example of a "staircase" sequence of states, such as those discussed in "devil's staircase" models [29] We note that, even if the actual sequence of states is not realized in the proposed manner (e.g., not infinite), our experimental observations already present a sequence of states with switchable band splitting: the $n = 1$ (no split), 2 (split polarized bands), ∞ (no split).

V. CONCLUSIONS

The presented results highlight the potential of using the dimerization phenomenon in heavy-element compounds for control of the electronic band polarization in nonmagnetic materials. The splitting of the bands into spin-polarized pairs can be switched on and off by either temperature or strain, using the combination of SOC and the switchable inversion symmetry of the dimerized crystal lattice. IrTe$_2$ itself remains metallic at all temperatures [10,11] and therefore might not serve as a prime candidate for the active (semiconducting) medium for spintronic or valleytronic applications [7,8], at least in its bulk form. Many other layered metal dichalcogenides are good semiconductors [7], and the properties of atomically thin layers could differ significantly from those of the bulk samples. Metal-metal dimerization is found in many transition metal compounds. The mechanism of band polarization control demonstrated in this paper opens a new search direction for functional electronic materials and emphasizes the potential of heavy-element compounds with large SOC for electronic applications.

APPENDIX

Here, we mark the structural phases using their modulation wave vectors $q_n = (1/p, 0, 1/p)$, with $p = 3n + 2$. Thus, the $n = 1$ phase is referred to as the $(1/5, 0, 1/5)$ phase, etc.

1. Construction of the unit cells

As described in the main text, unstrained unit cells were used for the DFT calculations involving relaxation of the

structures and testing their stability. The unstrained unit cell is tilted with respect to the high-T crystallographic axes in the same manner as the actual low-T unit cells shown in Figs. 1(g)–1(i). However, the atoms in the corner points in the unstrained cells retain their high-T positions (these atoms shift slightly in the actual low-T structures). In other words, the unstrained unit cells possess the same symmetry and orientation as the actual low-T unit cells, but are constructed on the atomic grid of the high-T structure. Inside the unstrained cells, the atoms can move in any manner.

Below, we give the linear transformation [30], Eqs. (A1a) and (A1b), between the high temperature unit cell lattice vectors $\mathbf{a}_0, \mathbf{b}_0, \mathbf{c}_0$ defined with respect to the origin O_0, and the low temperature unit cell lattice vectors $\mathbf{a}_{(1/p,0,1/p)}, \mathbf{b}_{(1/p,0,1/p)}, \mathbf{c}_{(1/p,0,1/p)}$ of the unstrained cell defined with respect to a new origin O (shifted by a vector $\mathbf{p}_{(1/p,0,1/p)}$ with respect to O_0). To determine these matrices, we imposed the following constrains: (i) the unit cell should give supercell Bragg peaks with the periodicity $(1/p, 0, 1/p)$ with respect to the high temperature reciprocal space, (ii) the symmetry should be monoclinic [triclinic for the case of the $(1/5, 0, 1/5)$ and $(1/10, 0, 1/10)$ structures], and (iii) one of the three lattice vectors of the $(1/p, 0, 1/p)$ phase should point in the direction of the dimer stripe.

$$\left[\mathbf{a}_{(\frac{1}{p},0,\frac{1}{p})}, \mathbf{b}_{(\frac{1}{p},0,\frac{1}{p})}, \mathbf{c}_{(\frac{1}{p},0,\frac{1}{p})}\right] = (\mathbf{a}_0,\mathbf{b}_0,\mathbf{c}_0)\,\{P\}_{(\frac{1}{p},0,\frac{1}{p})} \quad \text{(A1a)}$$

$$\mathbf{p}_{(\frac{1}{p},0,\frac{1}{p})} = (\mathbf{a}_0,\mathbf{b}_0,\mathbf{c}_0)\,\{p\}_{(\frac{1}{p},0,\frac{1}{p})} \quad \text{(A1b)}$$

$$\{P\}_{(\frac{1}{p},0,\frac{1}{p})} = \begin{Bmatrix} P_{11} & P_{12} & P_{13} \\ P_{21} & P_{22} & P_{23} \\ P_{31} & P_{32} & P_{33} \end{Bmatrix} \quad \text{(A2a)}$$

$$\{p\}_{(\frac{1}{p},0,\frac{1}{p})} = \begin{Bmatrix} p_1 \\ p_2 \\ p_3 \end{Bmatrix} \quad \text{(A2b)}$$

For example, in the case of the $(1/5, 0, 1/5)$ phase, using the high temperature lattice parameters $|\mathbf{a}_0| = |\mathbf{b}_0| = 3.9295$ Å, $|\mathbf{c}_0| = 5.3984$ Å and the following linear transformation (with no origin shift),

$$\left[\mathbf{a}_{(\frac{1}{5},0,\frac{1}{5})}, \mathbf{b}_{(\frac{1}{5},0,\frac{1}{5})}, \mathbf{c}_{(\frac{1}{5},0,\frac{1}{5})}\right] = (\mathbf{a}_0, \mathbf{b}_0, \mathbf{c}_0) \begin{Bmatrix} 0 & -1 & 4 \\ 1 & -1 & 2 \\ 0 & 1 & 1 \end{Bmatrix}$$
$$\text{(A3)}$$

one obtains the unstrained lattice parameters $|\mathbf{a}_{(1/5,0,1/5)}| = 3.9295$ Å, $|\mathbf{b}_{(1/5,0,1/5)}| = 6.6771$ Å, $|\mathbf{c}_{(1/5,0,1/5)}| = 14.64357$ Å, $\alpha_{(1/5,0,1/5)} = 100.119°$, $\beta_{(1/5,0,1/5)} = 90°$, $\gamma_{(1/5,0,1/5)} = 107.112°$. These parameters are only slightly different from the experimentally measured lattice parameters 3.9548(2) Å, 6.6542(4) Å, 14.4345(7) Å, 98.129(5)°, 92.571(4)°, and 107.119(5)°. Similarly, the corresponding differences between the experimental and the unstrained cells were small in all the other cases considered, justifying the use of the unstrained cells in our calculations.

The same matrix $\{P\}_{(1/p,0,1/p)}$ can be used to transform the coordinates of a point from the reciprocal space of the high temperature phase, (h_0,k_0,l_0) to a point $[h, k, l]$ from the

reciprocal space of the $(1/p, 0, 1/p)$ phase:

$$[h, h, l]_{(\frac{1}{p}, 0, \frac{1}{p})} = (h_0, k_0, l_0)\{P\}_{(\frac{1}{p}, 0, \frac{1}{p})} \quad \text{(A4)}$$

The following matrices are used to transform the atomic coordinates (x_0, y_0, z_0) of an atom from the high temperature unit cell to the atomic coordinates $[x, y, z]$ of an atom from the unit cell corresponding to the $(1/p, 0, 1/p)$ phase:

$$\begin{bmatrix} x \\ y \\ z \end{bmatrix}_{(\frac{1}{p},0,\frac{1}{p})} = \{Q\}_{(\frac{1}{p},0,\frac{1}{p})}\begin{pmatrix} x_0 \\ y_0 \\ z_0 \end{pmatrix} + \{q\}_{(\frac{1}{p},0,\frac{1}{p})} \quad \text{(A5)}$$

$$\{Q\}_{(\frac{1}{p},0,\frac{1}{p})} = \{P\}^{-1}_{(\frac{1}{p},0,\frac{1}{p})} \quad \text{(A6a)}$$

$$\{q\}_{(\frac{1}{p},0,\frac{1}{p})} = -\{P\}^{-1}_{(\frac{1}{p},0,\frac{1}{p})}\{p\}_{(\frac{1}{p},0,\frac{1}{p})} \quad \text{(A6b)}$$

Below, we list the matrices used to obtain the supercell unit cells corresponding to the dimerized phases considered in our work:

$$\left.\begin{matrix} \text{D3} \\ \text{D3}\underline{\text{D3}} \\ \text{D4}\underline{\text{D2}} \\ \text{D5}\underline{\text{D1}} \end{matrix}\right\} \{P\}_{(\frac{1}{10},0,\frac{1}{10})} = \begin{Bmatrix} 0 & -1 & 8 \\ 1 & -1 & 4 \\ 0 & 1 & 2 \end{Bmatrix} \quad \text{(A7)}$$

$$\left.\begin{matrix} \text{D2} \\ \text{D1}\underline{\text{D3}} \\ \text{D2}\underline{\text{D2}} \\ \text{D1}\underline{\text{D3}} \end{matrix}\right\} \{P\}_{(\frac{1}{8},0,\frac{1}{8})} = \begin{Bmatrix} -2 & 0 & 6 \\ -1 & -1 & 3 \\ 2 & 0 & 2 \end{Bmatrix} \quad \text{(A8)}$$

$$\text{D1D1D3}\}\{P\}_{(\frac{1}{11},0,\frac{1}{11})} = \begin{Bmatrix} 2 & 0 & 8 \\ 1 & 1 & 4 \\ -2 & 0 & 3 \end{Bmatrix} \quad \text{(A9)}$$

$$\left.\begin{matrix} \text{D2}\underline{\text{D1}} \\ \text{D3}\underline{\text{D1}}\text{D1}\underline{\text{D1}} \end{matrix}\right\}\{P\}_{(\frac{1}{14},0,\frac{1}{14})} = \begin{Bmatrix} 2 & 0 & 10 \\ 1 & 1 & 5 \\ -2 & 0 & 4 \end{Bmatrix} \quad \text{(A10)}$$

$$\left.\begin{matrix} \text{D1} \\ \text{D1}\underline{\text{D1}} \end{matrix}\right\}\{P\}_{(\frac{1}{6},0,\frac{1}{6})} = \begin{Bmatrix} 2 & 0 & 4 \\ 1 & 1 & 2 \\ -2 & 0 & 2 \end{Bmatrix} \quad \text{(A11)}$$

$$\left.\begin{matrix} \text{D} \\ \text{D}\underline{\text{D}} \end{matrix}\right\}\{P\}_{(\frac{1}{4},0,\frac{1}{4})} = \begin{Bmatrix} 2 & 0 & 2 \\ 1 & 1 & 1 \\ -2 & 0 & 2 \end{Bmatrix} \quad \text{(A12)}$$

The matrix corresponding to the origin shift is zero for all the phases, apart from the $(1/6, 0, 1/6)$ phase which has the following origin shift:

$$\{p\}_{(\frac{1}{6},0,\frac{1}{6})} = \begin{Bmatrix} 0 \\ 0 \\ \frac{1}{2} \end{Bmatrix} \quad \text{(A13)}$$

The most reliable results for comparison of the total energies of different dimer patterns with the same fraction of the dimerized Ir atoms are obtained when the same unit cell is used in the calculations. Thus, even though the dimer pattern D3 can be constructed in the unstrained unit cell corresponding to the $(1/5, 0, 1/5)$ phase, for the theoretical calculations it was stabilized in the larger unstrained unit cell corresponding to the $(1/10, 0, 1/10)$ phase. The obtained total energy could then

be reliably compared to the energies of the other three dimer arrangements having the same dimer density, but exhibiting the (1/10, 0, 1/10) modulation (see Fig. 3). The same was done for the other dimer patterns: the (1/8, 0, 1/8) cell was used instead of the smallest possible (1/4, 0, 1/4) cell for the dimer pattern D2, (1/14, 0, 1/14) was used for D2$\underline{D}$1 instead of (1/7, 0, 1/7), (1/6, 0, 1/6) instead of (1/3, 0, 1/3) for D1, and (1/4, 0, 1/4) instead of (1/2, 0, 1/2) for D. Stabilizing the same dimer patterns in such enlarged unit cells gave the identical arrangements of the atoms relative to each other.

2. Total energies

Total energies were calculated using several different approximations (LDA [26] and GGA-PBE [25], with and without spin-orbit coupling included), using two different codes: VASP [27] and WIEN2k [24]. The crystallographic structures used for the calculations are those given in Tables I and III for the (1/8, 0, 1/8) and the (1/6, 0, 1/6) states, respectively. The crystallographic structure for the (1/5, 0, 1/5) state was taken from Ref. [12]. The primitive unit cell (room temperature) containing one formula unit (f.u.) per unit cell, used as a reference in our calculations is space group 164, $a = 3.92990$ Å, $c = 5.39510$ Å, atomic position Ir $(1a) = (0, 0, 0)$, and Te $(1d) = (1/3, 2/3, 0.25350)$. We consider the

differences ΔE between the total energies of the dimerized structures $E_{(1/p,0,1/p)}$ and the total energy of the room-temperature structure E_0,

$$\Delta E_{(\frac{1}{p}, 0, \frac{1}{p})} = \frac{E_{(\frac{1}{p}, 0, \frac{1}{p})}}{\text{Number of f.u.}} - E_0(\text{primitive unit cell}),$$

$$(A14)$$

calculated per f.u. Below, the results obtained using VASP are given. No SOC, GGA-PBE: $\Delta E_{(1/5,0,1/5)} = -3.5$ meV, $\Delta E_{(1/8,0,1/8)} = -7.6$ meV, $\Delta E_{(1/6,0,1/6)} = 71.1$ meV. No SOC, LDA: $\Delta E_{(1/5,0,1/5)} = -16.4$ meV, $\Delta E_{(1/8,0,1/8)} = -32.4$ meV, $\Delta E_{(1/6,0,1/6)} = -6.5$ meV. Spin-orbit coupling included, GGA-PBE: $\Delta E_{(1/5,0,1/5)} = 15.10$ meV, $\Delta E_{(1/8,0,1/8)} = 20.60$ meV, $\Delta E_{(1/6,0,16)} = 104.7$ meV. Spin-orbit coupling included, LDA: $\Delta E_{(1/5,0,1/5)} = 2.5$ meV, $\Delta E_{(1/8,0,1/8)} = -3.8$ meV, $\Delta E_{(1/6,0,1/6)} = 27.6$ meV. Here, ΔE were also calculated using WIEN2k code (for the same unit cells and atomic positions), and the same trends were obtained. These results indicate that the considered DFT methods do not correctly predict the ground state of the system because they favor the undistorted state over the dimerized structures. Thus, more advanced numerical techniques should be used for that purpose, as described in the main text.

[1] B. J. Kim, H. Ohsumi, T. Komesu, S. Sakai, T. Morita, H. Takagi, and T. Arima, Science **323**, 1329 (2009).

[2] M. Z. Hasan and C. L. Kane, Rev. Mod. Phys. **82**, 3045 (2010).

[3] E. I. Rashba, Sov. Phys. Solid Sate **2**, 1109 (1960).

[4] S. Datta and B. Das, Appl. Phys. Lett. **56**, 665 (1990).

[5] L. P. Gorkov and E. I. Rashba, Phys. Rev. Lett. **87**, 037004 (2001).

[6] J. Sinova, D. Culcer, Q. Niu, N. A. Sinitsyn, T. Jungwirth, and A. H. MacDonald, Phys. Rev. Lett. **92**, 126603 (2004).

[7] X. Xu, W. Yao, D. Xiao, and T. F. Heinz, Nat. Phys. **10**, 343 (2014).

[8] Y. J. Zhang, T. Oka, R. Suzuki, J. T. Ye, and Y. Iwasa, Science **344**, 725 (2014).

[9] K. Ishizaka, M. S. Bahramy, H. Murakawa, M. Sakano, T. Shimojima, T. Sonobe, K. Koizumi, S. Shin, H. Miyahara, A. Kimura *et al.*, Nat. Mater. **10**, 521 (2011).

[10] S. Jobic, P. Deniard, R. Brec, J. Rouxel, A. Jouanneaux, and A. N. Fitch, Z. Anorg. Allg. Chem. **598**, 199 (1991).

[11] J. J. Yang, Y. J. Choi, Y. S. Oh, A. Hogan, Y. Horibe, K. Kim, B. I. Min, and S. W. Cheong, Phys. Rev. Lett. **108**, 116402 (2012).

[12] G. L. Pascut, K. Haule, M. J. Gutmann, S. A. Barnett, A. Bombardi, S. Artyukhin, T. Birol, D. Vanderbilt, J. J. Yang, S.-W. Cheong, and V. Kiryukhin, Phys. Rev. Lett. **112**, 086402 (2014).

[13] P.-J. Hsu, T. Mauerer, M. Vogt, J. J. Yang, Y. S. Oh, S.-W. Cheong, M. Bode, and W. Wu, Phys. Rev. Lett. **111**, 266401 (2013).

[14] A. F. Fang, G. Xu, T. Dong, P. Zheng, and N. L. Wang, Sci. Rep. **3**, 1153 (2013).

[15] H. Cao, B. C. Chakoumakos, X. Chen, J. Yan, M. A. McGuire, H. Yang, R. Custelcean, H. Zhou, D. J. Singh, and D. Mandrus, Phys. Rev. B **88**, 115122 (2013).

[16] D. Ootsuki, S. Pyon, K. Kudo, M. Nohara, M. Horio, T. Yoshida, A. Fujimori, M. Arita, H. Anzai, H. Namatame, M. Taniguchi, N. L. Saini, and T. Mizokawa, J. Phys. Soc. Jpn. **83**, 033704 (2014).

[17] N. Matsumoto, K. Taniguchi, R. Endoh, H. Takano, and S. Nagata, J. Low Temp. Phys. **117**, 1129 (1999).

[18] Y. S. Oh, J. J. Yang, Y. Horibe, and S.-W. Cheong, Phys. Rev. Lett. **110**, 127209 (2013).

[19] CrysAlisPro, Oxford Diffraction Ltd., Version 1.171.36.28.

[20] L. Palatinus and G. J. Chapuis, J. Appl. Cryst. **40**, 786 (2007).

[21] V. Petricek, M. Dusek, and L. Palatinus, Jana2006—*Structure Determination Software Programs* (Institute of Physics, Prague, Czech Republic, 2006).

[22] K. Momma and F. Izumi, J. Appl. Crystallogr. **44**, 1272 (2011).

[23] R. C. Clark and J. S. Reid, Acta Cryst. A **51**, 887 (1995).

[24] P. Blaha, K. Schwartz, G. Madsen, D. Kvasnicka, and J. Luitz, WIEN2k: *An Augmented Plane Wave + LO Program for Calculating Crystal Properties* (TU Wien, Vienna, 2001).

[25] J. P. Perdew, K. Burke, and M. Ernzerhof, Phys. Rev. Lett. **77**, 3865 (1996).

[26] J. P. Perdew and A. Zunger, Phys. Rev. B **23**, 5048 (1981).

[27] P. E. Blochl, Phys. Rev. B **50**, 17953 (1994); G. Kresse and D. Joubert, *ibid.* **59**, 1758 (1999).

[28] W. H. Baur, Acta Cryst. B **30**, 1195 (1974).

[29] P. Bak, Rep. Progr. Phys. **45**, 587 (1982).

[30] *Volume A, Space-Group Symmetry*, 5th ed., edited by Th. Hahn (Kluwer Academic Publishers, Dordrecht, 2002).